Semiclassical theory for liquidlike behavior of the frustrated magnet $Ca_{10}Cr_7O_{28}$

Sounak Biswas and Kedar Damle
Tata Institute of Fundamental Research, 1 Homi Bhabha Road, Mumbai 400005, India

(Received 16 July 2017; revised manuscript received 23 November 2017; published 1 March 2018)

We identify the low energy effective Hamiltonian that is expected to describe the low temperature properties of the frustrated magnet $Ca_{10}Cr_7O_{28}$. Motivated by the fact that this effective Hamiltonian has $S = 3/2$ effective moments as its degrees of freedom, we use semiclassical spin-wave theory to study the $T = 0$ physics of this effective model and argue that singular spin-wave fluctuations destabilize the spiral order favored by the exchange couplings of this effective Hamiltonian. We also use a combination of classical Monte-Carlo simulations and molecular dynamics, as well as analytical approximations, to study the physics at low, nonzero temperatures. The results of these nonzero temperature calculations capture the liquidlike structure factors observed in the temperature range accessed by recent experiments. Additionally, at still lower temperatures, they predict that a transition to nematic order in the bond energies reflects itself in the spin channel in the form of a crossover to a regime with large but finite correlation length for spiral spin correlations and a corresponding slowing down of spin dynamics.

DOI: 10.1103/PhysRevB.97.115102

I. INTRODUCTION

At a phenomenological level, spin liquids are magnetic materials which avoid ordering down to the lowest temperatures studied, well below the temperature scale set by the exchange interactions. This sets them apart from most other magnetic materials which order at the temperature scale of the exchange interactions. This negative characterization of a spin liquid, although rooted in experimental phenomenology, is of limited utility from a theoretical point of view. A lot of theoretical effort over the years has therefore been devoted to a more positive characterization of spin liquid phases, in terms of topological order, emergent gauge structure, and fractional excitations [1,2].

Systems with geometrically frustrated antiferromagnetic interactions, which result in a macroscopic degeneracy of low-energy configurations that minimize the (classical) energy, are natural candidates for spin liquid behavior. One example is the frustrated magnet SCGO ($SrCr_{9p}Ga_{12-9p}O_{19}$), which serves as a paradigmatic example of a classical spin liquid, in which the observed behavior can be explained in terms of the macroscopic degeneracy of ground states of $S = 3/2$ moments on the SCGO lattice in the classical limit, with the effects of thermal fluctuations and nonmagnetic impurities also accounted for within this classical approximation [3–6]. Other examples include minerals such as Herbertsmithite and Volborthite, and organic solids like κ-$(ET)_2Cu_2(CN)_3$, which are well-studied candidates for quantum spin liquid behavior [1,7,8].

Recently, Balz *et al.* [9,10] added to this list of candidates with a report of spin liquid behavior in the compound $Ca_{10}Cr_7O_{28}$. In $Ca_{10}Cr_7O_{28}$, the spin $S = 1/2$ Cr^{5+} ions form magnetically isolated Kagome bilayers. Using high field data on the one-magnon (single spin flip) excitation spectrum above the fully-polarized ground state, Balz *et al.* [9,10] have argued that the magnetic Hamiltonian consists of nearest-neighbor Heisenberg exchange couplings in each Kagome layer of the bilayer, as well as ferromagnetic exchange couplings between the two layers that make up each bilayer. A key feature of the exchange couplings extracted from their analysis is the following: In each bilayer, the up (down) pointing triangles of the lower (upper) Kagome layer host relatively large *ferromagnetic* exchange couplings, while the down (up) pointing triangles of the lower (upper) Kagome layer host significantly smaller antiferromagnetic exchange couplings roughly equal in magnitude to the ferromagnetic exchange interactions that couple the upper and lower Kagome layers to each other (see Fig. 1). One of the reasons for the recent interest in $Ca_{10}Cr_7O_{28}$ is the fact that spin liquid behavior is observed in spite of the dominant ferromagnetic couplings [9,10].

Here, we provide an alternative theoretical perspective that relates the low temperature physics of $Ca_{10}Cr_7O_{28}$ to the semiclassical large-spin limit of honeycomb lattice antiferromagnets with frustrating next-nearest neighbor couplings. Our starting point is the following simple observation: Since the dominant intralayer ferromagnetic couplings are at least three times larger in magnitude compared to the intralayer antiferromagnetic and interlayer ferromagnetic couplings [9,10], it should be possible to obtain a fairly accurate description of the low energy part of the spectrum by working with effective $S = 3/2$ degrees of freedom that represent the total spin of ferromagnetically coupled up (down) pointing triangles of the lower (upper) Kagome layer in each bilayer (see Fig. 1). We expect this crucial simplification to be valid below a temperature scale set by the magnitude of these dominant intralayer ferromagnetic couplings. Since $S = 3/2$ magnets can usually be described in classical terms fairly well (except possibly at ultra-low temperatures which the experiments of Balz *et al.* do not access), this observation immediately opens the door to a semiclassical treatment [11,12] of the problem.

As will be clear below, the pattern of exchange couplings extracted by Balz *et al.* from their analysis of the high-field data implies that these $S = 3/2$ degrees of freedom can be

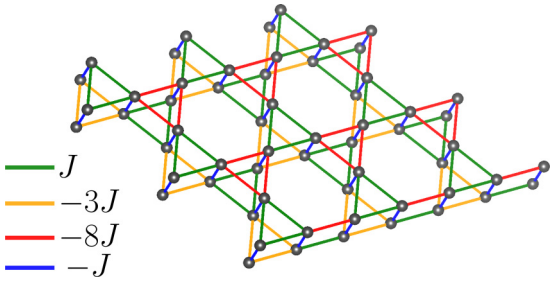

FIG. 1. The Cr^{5+} ions in $Ca_{10}Cr_7O_{28}$ form a Kagome bilayer structure, as reported in Ref. [9]. Each layer has antiferromagnetic couplings $\simeq J = 0.1$ meV as well as much stronger ferromagnetic couplings, as indicated in the figure, while the interlayer couplings are again antiferromagnetic with magnitude $\simeq J = 0.1$ meV. Green and red links constitute the upper Kagome layer, while green and yellow links constitute the lower Kagome layer. Blue links denote interlayer couplings. This figure has been created using VESTA [13].

thought of as occupying sites of a *honeycomb lattice* with nearest-neighbor ferromagnetic exchange couplings (J_1) and next-nearest-neighbor antiferromagnetic exchange couplings (J_2) of roughly equal magnitude. In our work here, we perform a semiclassical analysis of the properties of this honeycomb lattice model, with a view towards understanding the liquidlike behavior observed in experiments at not-too-low temperature [9,10]. Our basic conclusion is that such a semiclassical description reproduces the observed liquidlike structure factors seen in the temperature range accessed by recent experiments on $Ca_{10}Cr_7O_{28}$. Additionally, our results predict a lower temperature crossover to a regime with large but finite correlation length for spiral spin correlations and a corresponding increase in spin autocorrelation times. This crossover occurs at roughly the same temperature at which the bond energies are known to develop nematic order [14]. This onset of nematicity in the bond energies is also related to the observed threefold symmetry breaking phase transition seen in the work of Okumura *et al.* [15] in the classical model in a different parameter regime of J_2/J_1.

The physical picture that emerges from our analysis is as follows: The effective spin $S = 3/2$ moments can minimize their classical exchange energy by forming *spiral* states at any wave vector $\vec{q}$ that falls on a one-dimensional locus $\mathbf{Q}_s$ in reciprocal space. The leading $1/S$ corrections about any such classical spiral state labeled by $\vec{q}$ consist of two bands of harmonic spin-wave fluctuations. Including the zero point energy of these spin waves selects a spiral with a specific set of zone-boundary wave vectors that minimizes this leading $1/S$ correction to the ground state energy. However, the energy $E_-(\vec{k})$ of the lower band of spin waves vanishes whenever $\vec{k}$ approaches any point on the entire one-dimensional locus of spiral wave vectors $\mathbf{Q}_s$ (in addition to vanishing at wave vector $\vec{k} = 0$). Within this harmonic theory of spin-wave fluctuations, this vanishing of $E_-(\vec{k})$ on the entire locus $\mathbf{Q}_s$ is crucially implicated in the *logarithmic divergence* of the mean-square amplitude of transverse fluctuations about any such classical spiral state.

This divergence of transverse fluctuations, reminiscent of the mechanism by which long range antiferromagnetic order is destroyed by spin wave fluctuations at $T = 0$ in *one-dimensional systems*, suggests (by analogy to this well-understood one dimensional case) that spiral order is likely destabilized by spinwave fluctuations at $T = 0$, although further analysis would be needed to account for possible subtleties arising from anharmonic (higher order in $1/S$) corrections to this picture. We return to a brief discussion of this point towards the end of this paper.

Of greater relevance to the experiments of Balz *et al.* is the effect of thermal fluctuations on this incipient spiral order. Our results show that thermal fluctuations lead, below a crossover temperature scale, to a regime with a large but finite correlation length for spiral correlations of the spins at a particular set of entropically-selected zone-boundary wave vector on the spiral locus $\mathbf{Q}_s$. Additionally, we find a characteristic increase in the spin relaxation times below this crossover temperature. These crossovers in the spin channel take place at roughly the same temperature as the sharp onset of nematic correlations in the bond energies studied in the work of Mulder *et al.* [14]. In this low temperature regime, a large but finite correlation length for spiral spin correlations thus coexists with nematicity in the bond energies. This relatively simple theoretical picture complements the more sophisticated pseudofermion functional renormalization group analysis employed by Balz *et al.* in their own theoretical analysis of the underlying microscopic model of $S = 1/2$ spins on the Kagome bilayer. Most of the inelastic neutron scattering results of Balz *et al.* are at temperatures above this crossover. In this regime, our calculations yield a liquidlike structure factor similar to these experimental results.

The rest of this paper is organized as follows. In Sec. II we introduce the microscopic model Hamiltonian extracted from high-field data on this calcium chromate compound [9,10] and identify the effective Hamiltonian that governs the behavior of the effective spin $S = 3/2$ degrees of freedom that represent the low energy degrees of freedom. In Sec. III, we carry out a large-N study of this effective model within the classical approximation (i.e., treating the $S = 3/2$ spins as fixed-length vectors of magnitude S) and calculate correlation functions and structure factors to leading order in large-N. In Sec. IV, motivated by our large-N results, we construct a degenerate set of spiral ground states (*Luttinger-Tisza spirals*) for the classical system, with spiral ordering wave vectors $\vec{q}$ lying on a one-dimensional locus $\mathbf{Q}_s$ in reciprocal space and study the effect of quantum-mechanical spin-wave fluctuations about these ground states to leading order in the $1/S$ expansion. In Sec. V, we study the effect of thermal fluctuations on the degenerate manifold of ground states in the classical limit. In Sec. VI, we carry out a combined Monte Carlo-molecular dynamics study of the statics and dynamics of the effective model of classical spins identified in Sec. II and present numerical results for the temperature dependence of structure factor, specific heat, susceptibility, and relaxation time. We close with a brief discussion of some outstanding issues in Sec. VII.

II. THE EFFECTIVE MODEL

The crystal structure and magnetic properties of the magnetic insulator $Ca_{10}Cr_7O_{28}$ were studied recently by Balz *et al.* [9,10] using x-ray diffraction and inelastic neutron scattering methods as well as thermodynamic measurements. The magnetic Cr^{5+} ions ($S = 1/2$) were found to form Kagome

bilayers, with each bilayer magnetically isolated from the next by the absence of exchange pathways. Using inelastic neutron scattering at high magnetic fields, it was possible to map out the excitation spectrum of single spin-flip "magnon" excitations above the fully-polarized high-field ground state. The form of the microscopic Hamiltonian governing the dynamics of the $S = 1/2$ Kagome bilayers was deduced from fits to this data in conjunction with thermodynamic measurements. This analysis yielded the best-fit Hamiltonian

$$H(\vec{S}_i) = \sum_{ij} M_{ij}^{\text{bare}} \vec{S}_i . \vec{S}_j . \tag{1}$$

The isotropic Heisenberg exchange couplings that make up the matrix M_{ij}^{bare} above may be described as follows: Up-pointing (down-pointing) triangles of the lower (upper) Kagome layer in each bilayer consist of three spins strongly coupled to each other by strong ferromagnetic bonds of magnitude J_{ll}^F (J_{uu}^F), while the exchange couplings that constitute the links of down-pointing (up-pointing) triangles in the lower (upper) Kagome layer are antiferromagnetic, with a significantly smaller magnitude J_{ll}^{AF} (J_{uu}^{AF}). Additionally, spins directly above one another are connected by a ferromagnetic exchange interaction that couples the two layers of each Kagome bilayer. This has magnitude J_{ul}^F. To within the error bars quoted by Balz *et al.*, $J_{ll}^{AF} \simeq J_{uu}^{AF} \simeq J_{ul}^F \equiv J$, $J_{ll}^F \simeq 3J$, $J_{uu}^F \simeq 8J$, with $J \simeq 0.1$ meV. The magnetic lattice, as well as this pattern of exchange couplings, is displayed in Fig. 1.

As already noted by Ref. [9], the ferromagnetic exchange couplings J_{ll}^F and J_{uu}^F dominate over the antiferromagnetic couplings J_{ll}^{AF}, J_{uu}^{AF}, and J_{ul}^F, being at least three times larger than these antiferromagnetic couplings. Our starting point is the observation that low energy eigenstates are expected to be built from states in which the three spins coupled by J_{ll}^F (J_{uu}^F) in the lower (upper) Kagome layer are in a total spin $S_{\text{tot}} = 3/2$ state. This strongly suggests that the low energy physics should be described by an effective Hamiltonian written in terms of spin $S = 3/2$ moments that represent such strongly ferromagnetically coupled triangles. These strongly ferromagnetically coupled triangles in each Kagome layer thus form a triangular lattice of $S = 3/2$ moments, which represent states in the total spin $= 3/2$ multiplet of the three spin $S = 1/2$ moments coupled together by the strong ferromagnetic couplings acting within each such triangle. To obtain the effective interaction of these $S = 3/2$ effective moments with each other to leading order in the ratios of subleading couplings to the dominant ferromagnetic couplings, we must project these subleading couplings into the subspace of states obtained by restricting to the total spin $S = 3/2$ multiplet of each strongly coupled triangle. Performing this projection, we see that the $S = 3/2$ effective moments are coupled to each other by nearest neighbor antiferromagnetic Heisenberg exchange interactions of magnitude $J^{\text{eff}} = J/9$. In addition, to the same accuracy, the effect of the interlayer coupling J_{lu}^F is to introduce an effective ferromagnetic interlayer coupling of the same magnitude $J^{\text{eff}} = J/9$, which couples the two triangular layers of $S = 3/2$ moments. This is shown in Fig. 2. For the rest of this paper, we work with this effective model, which is expected to capture the physics correctly below a temperature scale set by the strong ferromagnetic couplings in each layer.

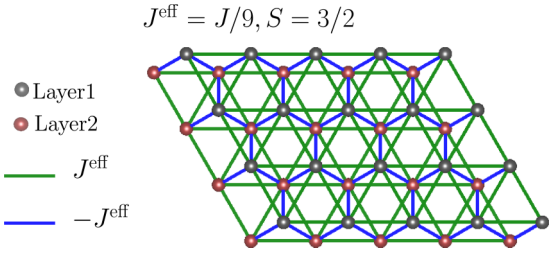

FIG. 2. The low energy effective Hamiltonian has spin $S = 3/2$ moments on a bilayer triangular lattice, with antiferromagnetic intralayer couplings and ferromagnetic interlayer couplings as shown. The magnitude of all couplings in this effective Hamiltonian is $J^{\text{eff}} = J/9$, where J is the microscopic in-plane antiferromagnetic coupling between the Cr^{5+} spins. This is equivalent to a honeycomb lattice with nearest-neighbor ferromagnetic couplings and next-nearest-neighbor antiferromagnetic couplings. When written in terms of unit vector $\hat{n}$ instead of vectors of length $S = 3/2$, the effective model has couplings of magnitude $J^{\text{eff}} S^2 \simeq 290$ mK $\simeq 0.025$ meV. Energies (frequencies) and temperatures are measured in units of this energy scale in all subsequent figures. This figure has been created using VESTA [13].

We note that features seen in experiments at temperatures of order this scale or higher cannot be reproduced correctly within this effective model for the low temperature physics. For instance, a bump at $T \simeq 4$ K in the experimental specific heat curve reported in Ref. [9] cannot be captured by calculations within this effective model. Nevertheless, the position of this bump corresponds quite well to the average of the two energy scales (since the ferromagnetic couplings in the two layers are different) associated with the unbinding of the ferromagnetically bound effective $S = 3/2$ moments into three $S = 1/2$ moments, suggesting that this is the origin of the specific heat feature studied experimentally. Since our calculations are in terms of an effective Hamiltonian for the spin $S = 3/2$ degrees of freedom, we do not capture this higher temperature feature within our effective theory.. In addition, high temperature calculations within the effective model will always yield a regime with an antiferromagnetic Curie-Weiss constant, rather than the ferromagnetic Curie-Weiss constant that characterizes the experimental high temperature susceptibility.

Finally, we note that this effective model of $S = 3/2$ moments on a bilayer triangular lattice is equivalent to a $J_1 - J_2$ Heisenberg model on a honeycomb lattice, with nearest neighbor ferromagnetic interactions $J_1 = J^{\text{eff}} = J/9$ (corresponding to the interlayer coupling between the two triangular layers that make up a bilayer) and next-nearest-neighbor antiferromagnetic interactions J_2 of the same magnitude (corresponding to the antiferromagnetic interaction between spin $S = 3/2$ moments on the same triangular layer). The spin-S $J_1 - J_2$ Heisenberg model on the honeycomb lattice has been the subject of several previous studies in the context of materials in the $BaM_2(XO_4)_2$ (M=Co, Ni; X= Pt, As) family and the $Bi_3M_4O_12(NO_3)$ family(M= Mn,V,Cr) [14–20], and we will make contact with these studies when we discuss our results. In our classical molecular dynamics and Monte Carlo studies, we choose to represent the classical $S = 3/2$ moments by unit vectors; this necessitates a rescaling of the exchange couplings by a factor of $|S|^2$, so that we work

with a model of unit vectors interacting with an exchange coupling of strength $J^{\text{eff}}|S|^2 = J/4$. For convenience, we quote all numerical values in units of $J/4$ or $(J/4)^{-1}$ in the rest of this paper ($J/4$ corresponds to approximately 0.025 meV or 290 mK).

III. LARGE-N STUDY

The problem of finding classical ground states given a pattern of exchange couplings is a constrained minimization problem. Instead of attacking it right away, we use the large-N approximation [21], whereby we generalize from the $O(3)$ degrees of freedom (in terms of which we write the classical limit of our spin Hamiltonian) to $O(N)$ vectors obeying the constraint $\vec{\phi}_i^2 = N$ on each site i, and then use the $N \to \infty$ solution to approximate the behavior at $N = 3$. This follows the path laid out by similar calculations for other frustrated classical spin systems [3,4,22–25].

When working within the large-N approximation, we choose to represent the $S = 3/2$ moments $\vec{S}$ as classical (c-number) vectors $\vec{\phi}$ of length $\sqrt{3}$ (instead of unit vectors that are a more convenient representation for our combined Monte Carlo and molecular dynamics computations). Thus we write $\vec{S} = \sqrt{3}\vec{\phi}/2$. In this language, the Hamiltonian is written as

$$H(\{\hat{n}_i\}) = (1/3)\sum_{ij} \vec{\phi}_i \cdot \vec{\phi}_j M_{ij}. \tag{2}$$

Here, M_{ij} is the pattern of couplings depicted in Fig. 2 with the exchange couplings J^{eff} rescaled by a factor of $|S|^2 = 9/4$, so that elements of M_{ij} have magnitude $J^{\text{eff}}S^2$ as alluded to in the end of the previous section. The additional prefactor of $1/3$ in Eq. (2) of course accounts for the rewriting in terms of vectors $\vec{\phi}$ of length $\sqrt{3}$.The lattice of Fig. 2 is a triangular Bravais lattice with a two-site unit cell representing the two layers of the original system. As noted in the previous section, it is equivalent, as far as the connectivity (not geometry) is concerned, to a honeycomb lattice with nearest and next-nearest-neighbor couplings. In Eq. (2) and all subsequent discussion we adopt the convention that i, j are composite indices comprised of the Bravais lattice site with coordinate $\vec{r}_i$, and a sublattice (layer) index α ($\alpha = 1,2$). When inessential, we suppress the sublattice indices in what follows.

The expression for the partition function in the large-N limit becomes

$$Z \propto \int \prod_i d\vec{\phi}_i \exp(-\beta H) \prod_i \delta\left(\vec{\phi}_i^2 - N\right). \tag{3}$$

Using $2\pi\delta(x) = \int d\lambda \exp(i\lambda x)$, and the expression for the Hamiltonian in Eq. (2), we can write the partition function [Eq. (3)] as

$$Z \propto \int \mathcal{D}[\lambda]\mathcal{D}[\vec{\phi}] \exp\left(iN\sum_i \lambda_i\right) \times \exp\left(-\sum_{ij} \vec{\phi}_i \cdot \vec{\phi}_j \left(\frac{\beta}{3} M_{ij} + i\lambda_i \delta_{ij}\right)\right), \tag{4}$$

where we have used $\mathcal{D}[\lambda] = \prod_i d\lambda_i$, and $\mathcal{D}[\vec{\phi}] = \prod_i d\vec{\phi}_i$. The λ_i integrals can be performed exactly using the fact that the saddle-point approximation becomes exact in the $N \to \infty$ limit. Setting all $\lambda_i = \lambda$, as is appropriate for a saddle-point that respects all lattice symmetries, one has

$$Z \propto \int \mathcal{D}[\vec{\phi}] \exp\left(-\frac{\beta}{3}\sum_{ij} \vec{\phi}_i \cdot \vec{\phi}_j (M_{ij} + \bar{\lambda}\delta_{ij})\right), \tag{5}$$

where $\bar{\lambda}$ is the saddle point value of $3i\lambda/\beta$, self-consistently determined by the equations

$$\langle \phi_i^2 \rangle_{\bar{\lambda}} = 1 \tag{6}$$

for each site i. Here ϕ_i is a scalar field that represents any one component of $\vec{\phi}_i$.

To find the lowest energy configurations that dominate the large-N path integral in the low temperature limit, we diagonalize the saddle point Hamiltonian matrix $M_{ij} + \bar{\lambda}\delta_{ij}$. We do this in Fourier space, where it is block diagonal. Our lattice is a triangular Bravais lattice with a two site unit cell. We introduce a sublattice index in the subscript of the scalar fields to write $\phi_\alpha(\vec{k}) = \sum_{r_i} \phi_{\alpha,r_i} \exp(-i\vec{k} \cdot \vec{r}_i)$. Here and in all subsequent discussion, wave vectors are measured in units of a^{-1} and positions in units of a, where a is the lattice spacing of the underlying triangular Bravais lattice, which we estimate to be $\simeq$5.35 A from the more precise measurements of the crystal structure given in Ref. [9,10] (small distortions from perfect Kagome bilayer geometry have been ignored in arriving at our estimate).

Here, α denotes the sublattice and the sum runs over unit cells. Expressing vectors in terms of their components along the principal axes $\hat{e}_1$ and $\hat{e}_2$ of the triangular lattice (with $\hat{e}_1 \cdot \hat{e}_2 = -1/2$), we have

$$\sum_{i,j} n_i M_{ij} n_j = \frac{1}{L^2}\sum_{\vec{k}} \Phi(\vec{k})^\dagger M(\vec{k}) \Phi(\vec{k}), \tag{7}$$

$$\Phi^\dagger(\vec{k}) = (\phi_1^*(\vec{k}), \phi_2^*(\vec{k})), \tag{8}$$

$$M(\vec{k}) = \frac{1}{2} J^{\text{eff}}|S|^2 \begin{pmatrix} \Delta & -K^* \\ -K & \Delta \end{pmatrix}, \tag{9}$$

where $\Delta = 2(\cos(k_1) + \cos(k_2) + \cos(k_1 + k_2))$ and $K = (1 + \exp(ik_1) + \exp(ik_1 + ik_2))$. The eigenvalues are given by $E^{\pm}(\vec{k}) = \frac{1}{2} J^{\text{eff}}|S|^2(\Delta \pm \sqrt{\Delta + 3})$.

These eigenvalues describe two dispersive bands. The lower band $E^-(\vec{k})$ has degenerate band minima labeled by wave vectors $\vec{q}$ such that

$$2(\cos(q_1) + \cos(q_2) + \cos(q_1 + q_2)) = -11/4. \tag{10}$$

The solutions of this equation lie on a locus $\mathbf{Q_s}$ shown in Fig. 3. It is worthwhile to compare this degeneracy with what one has as a result of large-N calculations for other frustrated systems which are known to exhibit spin-liquid behavior: $SrCr_{9p}Ga_{12-9p}O_{19}$, in which the lattice is a pyrochlore slab with nearest neighbor interactions, has a seven site unit cell and seven bands, of which the lowest three are flat. The pyrochlore lattice itself has, within this approximation, four bands, out of which the lower two are flat [22]. Herbertsmithite, where the spins are on a Kagome lattice, has three bands, out of which the lowest is flat [23]. Within large-N such flat bands are usually signatures of liquidlike behavior. Our line degeneracy is reminiscent of Volborthite [24] where the spins lie on a

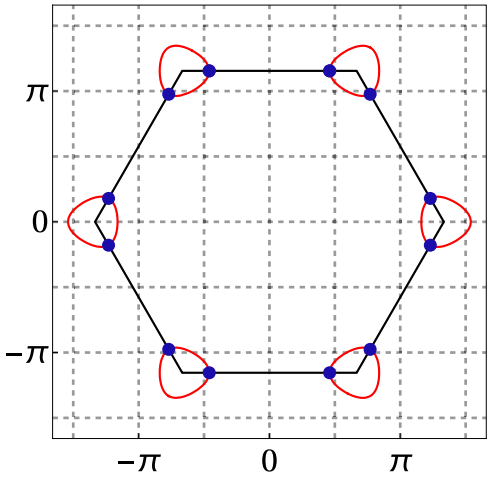

FIG. 3. Wave vectors labeling degenerate ground states lie on the locus $\mathbf{Q_s}$ marked in red. The hexagon marks the first Brillouin zone of the triangular Bravais lattice, and the x and the y axes refer to components of $\vec{q}$ in the $\hat{x}$ and $\hat{y}$ directions. Also marked are the points at the zone boundaries of the first Brillouin zone, which are selected by quantum fluctuations as well as thermal fluctuations (see main text for details).

distorted Kagome lattice and the lower band minima form a one-dimensional degenerate subspace.

The eigenvectors for any point $\vec{q}$ on this locus are given by $\phi^{\pm} = (\frac{1}{\sqrt{2}})(1, \mp \exp(i\theta_{\vec{q}}))$, where $\theta_{\vec{q}}$ is determined by

$$\cos(\theta_{\vec{q}}) = 2(1 + \cos(q_1) + \cos(q_1 + q_2))$$
$$\sin(\theta_{\vec{q}}) = 2(\sin(q_1) + \sin(q_1 + q_2)). \quad (11)$$

Note that the equation of the locus $\mathbf{Q_s}$ guarantees that this pair of equations for $\theta_{\vec{k}}$ has a legitimate solution.

Next, we calculate spin correlations in this large-N approximation by numerically solving Eq. (6) to obtain $\bar{\lambda}(\beta)$ and using this value to determine the equal time correlation function in momentum space. For a system of $L \times L$ unit cells, this is given by

$$\langle \phi_\alpha(\vec{k}) \phi_\beta(-\vec{k}') \rangle = L^2 \delta_{\vec{k},\vec{k}'} G_{\alpha,\beta}(\vec{k}), \quad (12)$$

$$G_{11}(\vec{k}) = G_{22}(\vec{k}) = \frac{3}{\beta} \frac{\Delta + \bar{\lambda}(\beta)}{(\Delta + \bar{\lambda}(\beta))^2 - (\Delta + 3)}, \quad (13)$$

$$G_{12}(\vec{k}) = G_{21}^*(\vec{k}) = \frac{3}{\beta} \frac{K}{(\Delta + \bar{\lambda}(\beta))^2 - (\Delta + 3)}. \quad (14)$$

In Fig. 4, we show the momentum-space correlation functions of spins in the same plane, $G_{11}(\vec{k})$, for two temperatures $T = 100$ mK and $T = 1$ K relevant to the experiments performed in Ref. [9]. One can also calculate the equal time spin structure factor within this approximation by using these results to compute

$$\mathcal{S}(\vec{k}) = \frac{1}{L^2} \langle |\phi_1(\vec{k}) f_1(\vec{k}) + \phi_2(\vec{k}) f_2(\vec{k})|^2 \rangle, \quad (15)$$

where the subscripts denote the sublattice as before, and $f_1(\vec{k})$ and $f_2(\vec{k})$ are the form factors for the bound $S = 3/2$ degrees of freedom corresponding to triangular plaquettes of ferromagnetically coupled spin 1/2 moments (see Appendix D).

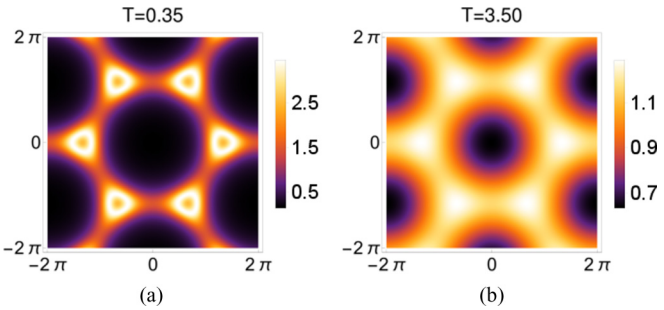

FIG. 4. In-plane momentum dependence (with out of plane momentum set to zero) of correlation functions of spins in the same plane, $G_{11}(\vec{k}) = G_{22}(\vec{k})$ [Eq. (13)], computed within the large-N approximation at temperatures (a) $0.35(J/4) \simeq 100$ mK and (b) $3.50(J/4) \simeq 1$ K ($(J/4) \simeq 290$ mK). The lower temperature results show clear features associated with the tendency towards spiral order.

In Fig. 5, we show the large-N results for the equal time structure factors at the same temperatures. The lower temperature scans at $T = 100$ mK clearly show features associated with the tendency towards spiral order, although there is clearly no true long range order possible in this two-dimensional system. We also note that the form factors partially smear out these "spiral features," making them harder to observe in the equal time spin structure factor (as opposed to the intraplane correlation function displayed earlier).

IV. SPIN-WAVE THEORY AT $T = 0$

From the large-N ground states obtained in the previous section, we may construct physical ground states of three-component vectors of magnitude $|S| = 3/2$. Since the eigenvectors of the exchange-coupling matrix M_{ij} have the same magnitude on both sublattices, it is possible to use these eigenvectors to construct valid classical ground states for the $S = 3/2$ spins. These are the 'Luttinger-Tisza' spiral ground states [26], obtained by making appropriate linear

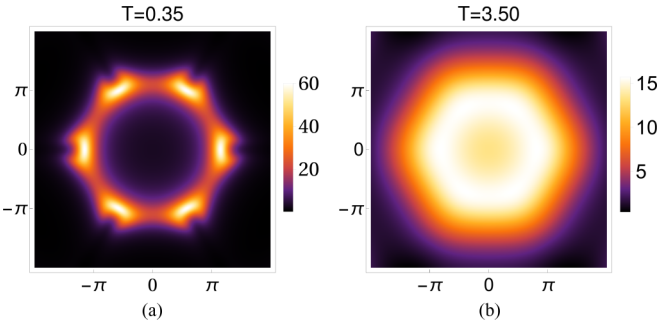

FIG. 5. In plane momentum dependence (with out of plane momentum set to zero) of the equal time structure factor of spins, $\mathcal{S}(\vec{k})$ [Eq. (15)] within the large-N approximation at two values of temperature: (a) $T = 0.35(J/4) \simeq 100$ mK and (b) $T = 3.50(J/4) \simeq 1$ K ($J/4 \approx 290$ mK). We note that form factors partially smear out, but do not eliminate the "spiral features" seen earlier (Fig. 4) in the intraplane spin correlations at the lower temperature.

combinations of the eigenvectors $\phi^{\pm}$:

$$\begin{aligned}\vec{S}_i^{\rm GS} &= |S|\hat{n}_i^{\rm GS}, \left(\hat{n}_i^{\rm GS}\right)^2 = 1,\\ \hat{n}_{1,r_i}^{\rm GS} &= (\cos(\vec{q}.\vec{r}_i)\hat{z} + \sin(\vec{q}.\vec{r}_i)\hat{x}),\\ \hat{n}_{2,r_i}^{\rm GS} &= (\cos(\vec{q}.\vec{r}_i - \theta_{\vec{q}})\hat{z} + \sin(\vec{q}.\vec{r}_i - \theta_{\vec{q}})\hat{x}),\end{aligned} \tag{16}$$

where $\vec{q}$ belongs to the ground-state manifold obtained from large-N results in Eq. (10) and we have used the explicit representation of the composite index i in terms of (α, r_i), where α is the sublattice index and r_i is the coordinate of the underlying triangular Bravais lattice. These classical ground states are related (by a spin flip on one sublattice) to those constructed by Mulder *et al.* in their study of the $S = 1/2$ honeycomb lattice J_1-J_2 with both couplings antiferromagnetic [14].

Now, we look at whether quantum fluctuations lift the degeneracy of the manifold of spiral ground states in (16) and whether they render such spiral ordering unstable. Although higher order corrections in $1/S$ (anharmonic corrections to the leading harmonic spin-wave theory) are outside the scope of our analysis, the leading order results may be expected to already be fairly reliable for spin $S = 3/2$. Some of our results in Sec. IV were obtained earlier in a different context in Ref. [16] and are reproduced here in the interests of a self-contained presentation. Our calculations are also analogous to similar spin-wave calculation by Mulder *et al.* [14] for the case of *antiferromagnetic* J_1, although there is no canonical transformation that connects the two problems, and the leading order spin-wave corrections (and the semiclassical spin dynamics) are therefore not the same although the classical ground states are closely related.

We consider spin-wave fluctuations about a spiral ordered state of Eq. (16) labeled by the wave vector $\vec{q}$ belonging to the degenerate ground-state locus $\mathbf{Q_s}$ given by Eq. (10). First, we rotate the local $\hat{z}$ axis to point along the spins in the spiral ordered state given by (16). This rotation transforms a generic quadratic term of our Heisenberg Hamiltonian in the following way:

$$\begin{aligned}\vec{S}_i.\vec{S}_j \rightarrow\ & S_i^y S_j^y + \left(S_i^z S_j^z + S_i^x S_j^x\right)\cos(\omega_{i,j})\\ &+ \left(S_i^z S_j^x - S_i^x S_j^z\right)\sin(\omega_{i,j}),\end{aligned} \tag{17}$$

where $\omega_{i,j}$ is given by

$$\begin{aligned}\omega_{i,j} &= \omega_{\alpha,r_i;\beta,r_j} = \vec{q}.(\vec{r}_i - \vec{r}_j) \text{ for } \alpha = \beta, \quad \text{and}\\ \omega_{1,r_i;2,r_j} &= -\omega_{2,r_j;1,r_i} = \vec{q}.(\vec{r}_i - \vec{r}_j) - \theta_{\vec{q}}.\end{aligned} \tag{18}$$

Here $\theta_{\vec{q}}$ is defined in Eq. (11), and we have explicitly expressed the composite indices i and j in terms of the sublattice index $\alpha,\beta = 1,2$ and the unit cell position coordinates r_i, r_j. Next, we choose the spin quantization axis along the local $\hat{z}$ axis defined above and make a transformation to Holstein-Primakoff bosons $b_{\alpha,i}, b_{\alpha,i}^{\dagger}$, in effect making the substitutions $S^z \rightarrow S - b^{\dagger}b$, $S^+ \rightarrow \sqrt{2S}b$, and $S^- \rightarrow \sqrt{2S}b^{\dagger}$ (correct to quadratic order). We then expand the resulting expansions to leading order in $1/S$, again keeping terms only up to quadratic order in the boson creation and annihilation operators, to obtain a noninteracting spin-wave Hamiltonian $H_{\rm SW}(\vec{q})$.

To diagonalize the spin-wave Hamiltonian, we transform to Fourier space as $b_{\alpha}(\vec{k}) = \sum_i b_{\alpha,i}\exp(i\vec{k}.\vec{r}_i)$, α labeling the sublattice, to obtain

$$H_{\rm SW}(\vec{q}) = E^{\rm GS} + \frac{|S|}{L^2}{\sum_{\vec{k}}}' \mathbf{b}^{\dagger}(\vec{k})\mathbf{M}(\vec{q},\vec{k})\mathbf{b}(\vec{k}) - 2a(\vec{q},\vec{k}), \tag{19}$$

$$\mathbf{b}^{\dagger} = (b_1^{\dagger}(\vec{k}), b_2^{\dagger}(\vec{k}), b_1(-\vec{k}), b_2(-\vec{k})). \tag{20}$$

Here, $\sum'$ denotes a sum over half of the Brillouin zone. The expressions for $a(\vec{q},\vec{k})$ and for the matrix $\mathbf{M}(\vec{q},\vec{k})$ are given in Appendix A. $E^{\rm GS}$ is the spiral ground-state energy independent of $\vec{k}$ and $\vec{q}$, given in terms of the connectivity matrix M_{ij} by

$$E^{\rm GS} = \sum_{i,j} \hat{S}_i^{\rm GS}(\vec{q}) M_{ij} S_j^{\rm GS}(\vec{q}), \tag{21}$$

for any $\vec{q}$ in the spiral ground-state manifold $\mathbf{Q_s}$ defined by Eq. (10). The quadratic spin-wave Hamiltonian $H_{\rm SW}(\vec{q})$ can be diagonalized by making a canonical transformation to Bogoliubov quasiparticles $\gamma_{\pm}(\vec{k})$, which preserve the bosonic commutation relations $[\gamma_{\mu}(\vec{k}), \gamma_{\nu}^{\dagger}(\vec{k}')] = \delta_{\vec{k},\vec{k}'}\delta_{\mu,\nu}$ $(\mu,\nu = \pm)$ [27]. In terms of the Bogoliubov quasiparticles, one can write

$$\begin{aligned}H_{\rm SW}(\vec{q}) &= E_{\rm GS} + E^0(\vec{q})\\ &\quad + \frac{|S|}{L^2}\sum_{\vec{k}\in BZ,\sigma=\pm} E_{\sigma}^{\rm SW}(\vec{q},\vec{k})\gamma_{\sigma}^{\dagger}(\vec{k})\gamma_{\sigma}(\vec{k}).\end{aligned} \tag{22}$$

The spin-wave dispersions $E_{\pm}^{\rm SW}(\vec{q},\vec{k}) = E_{\pm}^{\rm SW}(\vec{q},-\vec{k})$ are detailed in Appendix A. We note that the lower band $E_{-}^{\rm SW}(\vec{k})$ has zero energy modes at the spiral wave vectors lying on the locus $\mathbf{Q_s}$ defined in Eq. (10), apart from a Goldstone mode at $k = 0$. The $\vec{q}$-dependent zero point energy of spin-wave fluctuations $E^0(\vec{q})$ is given by

$$E^0(\vec{q}) = \frac{|S|}{L^2}{\sum_{\vec{k}}}' (E_{+}^{\rm SW}(\vec{q},\vec{k}) + E_{-}^{\rm SW}(\vec{q},\vec{k}) - 2a(\vec{q},\vec{k})). \tag{23}$$

To obtain the state favored by spin-wave fluctuations, we minimize the zero-point energy $E^0(\vec{q})$ in Eq. (23) over the classical ground state spiral wave vectors given by Eq. (10). We find that $E^0(\vec{q})$ is minimized for

$$(q_1, q_2) = (\arccos(1/8), \pi - \arccos(3/4)) \tag{24}$$

and the other wave vectors related by lattice symmetries. Therefore, within noninteracting spin-wave theory, quantum fluctuations favor the spiral states given by Eq. (24) and other wave vectors related by lattice symmetries. The wave vectors favored by quantum fluctuations lying within the first Brillouin zone are shown in Fig. 3.

The Mermin-Wagner theorem rules out order at any finite temperature. The question of whether the system orders at zero temperature can be studied within spin-wave theory by looking at the expectation value of magnetization about the local $\hat{z}$ axis:

$$\frac{1}{2L^2}\left\langle \sum_{\alpha,i} S_{\alpha,r_i}^z \right\rangle = \frac{1}{2L^2}\sum_{\vec{k},\alpha}(S - \langle b_{\alpha}^{+}(\vec{k})b_{\alpha}(\vec{k})\rangle). \tag{25}$$

A small expectation value of the Holstein-Primakoff boson number $(1/2L^2)\sum_{\vec{k},\alpha}\langle b_{\alpha}^{+}(\vec{k})b_{\alpha}(\vec{k})\rangle$ would imply that the spiral ground state is stable to transverse fluctuations. We numerically evaluate $\langle b_{\alpha}^{+}(\vec{k})b_{\alpha}(\vec{k})\rangle^{-1}$ and find that it vanishes on

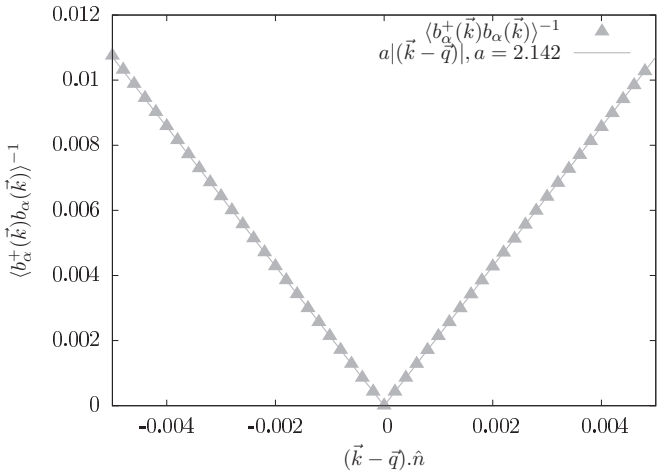

FIG. 6. The expectation value $\langle b_\alpha^+(\vec{k})b_\alpha(\vec{k})\rangle^{-1}$ calculated within leading-order spin wave theory. The plotted wave vectors are along $\hat{n}$, the local normal at a generic point on the locus $\mathbf{Q_s}$ of the degenerate spiral wave vectors given by Eq. (10). The solid line is a fit to the form $a|\vec{k}-\vec{q}|$, with $a = 2.142$. This linear behavior, being generic along the spiral locus, signifies an instability of the spiral order to transverse fluctuations (see main text for details).

the wave vectors belonging to the spiral manifold given by Eq. (10). For small deviations perpendicular to the locus of degenerate spiral wave vectors $\mathbf{Q_s}$, we find that $\langle b_\alpha^+(\vec{k})b_\alpha(\vec{k})\rangle^{-1} \propto |\vec{k}-\vec{q}|$ where $\vec{q}$ is any location on the spiral manifold. For a particular spiral wave vector $\vec{q}$, this linear dependence is shown in Fig. 6. We have checked that this linear behavior does not depend on the location of wave vector $\vec{q}$ on the spiral manifold given by Eq. (10). This linear behavior renders the integral $(1/2L^2)\sum_{\vec{k},\alpha}\langle b_\alpha^+(\vec{k})b_\alpha(\vec{k})\rangle$ logarithmically divergent in the thermodynamic limit. Within leading order spin-wave theory, we thus find that transverse fluctuations destabilize spiral order. We note that the spiral order suffers the same fate in the system with antiferromagnetic interlayer couplings [14], even though the spin-wave dispersions are different. (In this case, $\langle b_\alpha^+(\vec{k})b_\alpha(\vec{k})\rangle^{-1}$ is linear in perpendicular deviations $|\vec{k}-\vec{q}|$ with a different proportionality constant.) We note that the role of higher order terms in the $1/S$ needs to be analyzed to obtain a more definite prediction regarding the fate of the system. In spite of this caveat regarding the ultimate fate of the system, this analysis does strongly suggest that spiral order, favored by the pattern of exchange couplings in the system, is destabilized due by singular spin-wave fluctuations, possibly opening the door to $T = 0$ spin-liquid behavior. Another competing possibility is bond-energy nematic order of the type predicted for the $S = 1/2$ case in the work of Mulder *et al.* [14].

V. CLASSICAL FLUCTUATIONS ABOUT SPIRAL GROUND STATES

Having studied the effect of quantum fluctuations on classical ground states in Sec. IV, we now look at the effect of thermal fluctuations. Our method follows the one used in Ref. [28] in the analysis of the spinel $MnSc_2S_4$. A similar calculation has been reported earlier for a different regime of J_2/J_1 [15].

In this section, we work with configurations of unit vectors $\hat{n}$, such that $\vec{S} = |S|\hat{n}$. We consider fluctuations about the configuration $\hat{n}^{\rm GS}(\vec{q})$, where $\hat{n}^{\rm GS}(\vec{q})$ is the unit-vector configuration describing the spiral ground state $\vec{S}^{\rm GS}(\vec{q})$ defined in Eq. (16) and $\vec{q}$ belongs to the degenerate ground-state locus $\mathbf{Q_s}$. The configuration $\hat{n}_i$ can be written in terms of fields $\vec{\epsilon}_i$ describing fluctuations from $\hat{n}_i^{\rm GS}$ as

$$\hat{n}_i = \vec{\epsilon}_i + \hat{n}_i^{\rm GS}(\vec{q})\sqrt{1-\vec{\epsilon}_i^{\,2}}. \tag{26}$$

The fluctuation fields $\vec{\epsilon}_i$ satisfy $\vec{\epsilon}_i.\hat{n}_i^{\rm GS} = 0$ and are always constrained to obey $\vec{\epsilon}_i \leqslant 1$. Together with the form of Eq. (26), these conditions explicitly preserve the unit vector constraint on the spins. In terms of the fluctuation fields $\vec{\epsilon}$, one can write the partition function as

$$Z = \int \mathcal{D}[\hat{n}]\exp(-\beta H) \tag{27}$$

$$= \int \mathcal{D}[\epsilon]\exp(-\beta H)\prod_i \left(1-\vec{\epsilon}_i^{\,2}\right)^{-\frac{1}{2}}, \tag{28}$$

where we have put in the expression for the Jacobian of the transformation from the $\hat{n}_i$ to the $\vec{\epsilon}_i$ fields. The fluctuation fields $\vec{\epsilon}_i$ can be further decomposed into scalar fields π_i and ρ_i describing fluctuations in and out of the plane of the spiral as

$$\vec{\epsilon}_i = \rho_i\hat{y} + \pi_i(\hat{y}\times\vec{S}_i^{\,\rm GS}(\vec{q})). \tag{29}$$

We absorb the Jacobian into the exponential and express the partition function of Eq. (28) in terms of the scalar fields ρ and π using Eq. (26) and Eq. (29). Expanding in these fields and keeping terms up to quadratic order in ρ and π gives us the leading order partition function of small fluctuations about an ordered spiral ground state:

$$Z = \int \mathcal{D}[\pi]\mathcal{D}[\rho]\exp(-\mathcal{S}(\pi,\rho))$$

$$\mathcal{S} = \beta\sum_{ij}(\rho_i J_{ij}\rho_j + \pi_i K_{ij}\pi_j) - \frac{1}{2}\sum_i\left(\rho_i^2+\pi_i^2\right), \tag{30}$$

where the matrices J_{ij} and K_{ij} are defined in terms of the connectivity matrix M_{ij} of Eq. (2) and the spiral ground-state energy $E^{\rm GS}$ [Eq. (21)] as

$$J_{ij} = M_{ij} - E^{\rm GS}\delta_{ij},$$

$$K_{ij} = (M_{ij} - E^{\rm GS}\delta_{ij})\vec{S}_i^{\,\rm GS}(\vec{q})\cdot\vec{S}_j^{\,\rm GS}(\vec{q}). \tag{31}$$

We note that the in-plane fluctuation matrix K_{ij} has two bands as expected. The lower band has zeros exactly at the spiral wave vectors belonging to the degenerate ground state locus $\mathbf{Q_s}$ given by Eq. (10), i.e., it has a one-dimensional subspace of soft fluctuation modes (or zero modes), just like the connectivity matrix M_{ij}, apart from a zero mode at $\vec{k} = 0$.

Now, one can ask what states among the degenerate manifold of spiral ground states are entropically selected at nonzero but low temperatures. In this regime, one can drop the temperature independent Jacobian terms in the partition function of small fluctuations about the ordered spiral state $\vec{S}_i^{\,\rm GS}$. The fluctuation fields ρ and π can be integrated out

to give

$$Z(\vec{q}) = \int \mathcal{D}[\pi]\mathcal{D}[\rho] \exp\left(-\beta \sum_{ij} (\rho_i J_{ij} \rho_j + \pi_i K_{ij}(\vec{q}) \pi_j)\right)$$
$$\propto \det(\beta J)^{-1/2} \det(\beta K(\vec{q}))^{-1/2}, \quad (32)$$

where we have explicitly shown the dependence on the spiral wave vector $\vec{q}$. To find the states selected entropically, we minimize the free energy $F(\vec{q}) = -T \log(Z(\vec{q}))$ over the manifold of spiral states given by Eq. (10). The free energy, up to additive constants independent of temperature or the spiral wave vector q, is given by

$$F(\vec{q}) = \frac{1}{\beta} \mathrm{Tr}(\log(\beta J)) + \frac{1}{\beta} \mathrm{Tr}(\log(\beta K(\vec{q}))). \quad (33)$$

The first term is independent of the spiral wave vector $\vec{q}$ and cannot break the degeneracy of the ground states given by Eq. (10). As detailed in Appendix B, the trace in the second term can be easily calculated in the Fourier basis, where $K(\vec{q})$ is block diagonal. In this way, we find that the states selected by small fluctuations at small nonzero temperatures are the same as the ones selected at zero temperature by noninteracting spin waves, i.e., ones at the edges of the first Brillouin zone, given by Eq. (24) and shown in Fig. 3.

VI. NUMERICAL STUDY

In this section we undertake a combined Monte Carlo-molecular dynamics study of the classical effective spin 3/2 model described earlier.

A. Method

To study equilibrium properties and equal time correlation functions, we use Monte Carlo simulations. While embedded cluster algorithms are available for continuous spin systems [29,30], the extremely frustrated nature of the low temperature configurations of this model render these inefficient. Therefore, following Refs. [31] and [32], we use three single-spin updates: (a) *Over-relaxation* moves are energy-conserving microcanonical sweeps, which reflect the spin of each site about the effective magnetic field, (b) *heat-bath moves* to equilibrate each spin in the external exchange field of its neighbors, and (c) *parallel tempering*, which exchanges, with acceptance probability that obeys detailed balance, entire configurations between two independent simulations run at slightly different temperatures. More details on these update schemes can be found in Ref. [31]. For completeness, we have also documented the details relevant to our implementation in Appendix C.

To study the dynamics, we consider the classical Hamiltonian equations of motion, given by

$$|S| \frac{d\hat{n}_i}{dt} = \sum_j M_{ij} \hat{n}_j \times \hat{n}_i, \quad (34)$$

where $\hat{n}_i$ are unit vectors satisfying $\hat{n}_i^2 = 1$. The connectivity matrix M_{ij} is defined in Eq. (2) and given by the pattern of couplings in Fig. 2 with couplings rescaled by a factor of $|S|^2$. Following previous work on dynamics of spin models [11,12,33], we integrate the Hamiltonian equations of motion numerically using the fourth-order Runge-Kutta method. The time step of the numerical integrator is kept low enough to ensure the energy remains conserved to within the accuracy needed. In practice, we use a time step of $0.03(J/4)^{-1}$ to achieve this. To obtain the dynamical correlation functions, we integrate the Hamiltonian equations of motion starting from different initial configurations generated by the Monte Carlo simulation described in the previous paragraph. All quantities are averaged over initial conditions and the frequency dependence of observables is calculated by averaging Fourier transforms of the time evolution of the observable over this ensemble of initial conditions.

B. Results

The Mermin-Wagner theorem rules out the spontaneous breaking of any continuous symmetry in two dimensions, thereby ruling out any nonzero temperature regime with true long range spiral order in the spin correlations. However, discrete lattice symmetries can still be broken. Indeed, the work of Mulder *et al.* [14] has demonstrated an apparent transition to bond-energy nematic order for $J_2/J_1 = -1$ (and nearby values) in our notation, i.e., with both couplings antiferromagnetic (as far as the classical physics is concerned, the sign of J_1 can

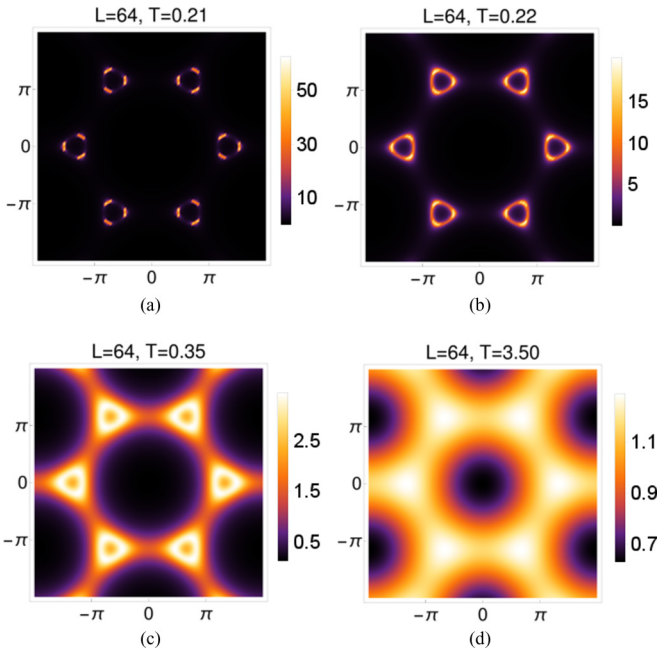

FIG. 7. Temperature and in-plane momentum dependence (with out of plane momentum set to zero) of the equal time correlation function of spins in the same layer (sublattice), obtained from classical Monte Carlo simulations of the effective model for a system of $L \times L$ unit cells with $L = 64$. (a) Data at $T = 0.20\,(J/4) \simeq 58$ mK shows clear evidence of the entropic selection of zone-boundary spiral wave vectors (see main text for details). (b) Data at a slightly higher temperature $T = 0.22\,(J/4) \simeq 64$ mK shows nearly equal intensity all along the locus of spiral wave vectors favored by the exchange interactions. (c) This weight along the locus of spiral wave vectors is already visible at a slightly higher temperature $T = 0.35\,(J/4) \simeq 100$ mK. (d) Finally, at an even higher temperature $T = 3.50 \simeq 1$ K, the momentum dependence has no sharp features ($J/4 \simeq 290$ mK).

be changed by flipping the spins on one sublattice, connecting this result to the case of interest to us). A similar transition had also been reported earlier in the literature by Okumura *et al.* [15] for $J_2/J_1 > -1/2$ (in our notation). While this transition was seen to be accompanied by the expected singular behavior of the specific heat in the cases studied by Okumura *et al.*, Mulder *et al.*'s results suggested that the specific heat does not scale at the nematic transition in the regime of J_2/J_1 studied by them [14,15].

From the point of view of the experiments that form our motivation, it is important to ask what are the signatures in the spin channel of this puzzling onset of bond-energy nematicity at $J_2/J_1 = 1$? To address this question, we study the effective model on triangular lattices with $L \times L$ unit cells, with each unit cell having two basis spins, and obtain the spin correlators, uniform spin susceptibility and the local spin autocorrelation function in the low temperature regime.

First, we look at the Fourier transformed correlation function of spins in the same plane $\langle n_\alpha(\vec{k}) n_\alpha(-\vec{k})\rangle_{\rm MC}$, obtained easily in our Monte Carlo simulations by fast Fourier transforming the spin configurations. At low temperature below a crossover scale $T_{\rm crossover} \simeq 0.22\,(J/4) \simeq 64$ mK, we see clear evidence for slowly decaying spiral correlations at wave vectors that form a one-dimensional locus in q space. In fact, this tendency becomes gradually visible starting at somewhat higher temperatures. When the temperature is lowered below this crossover scale, order-by-disorder effects apparently start preferring a particular set of zone boundary spiral wave vectors from this locus of degenerate spirals [Fig. 7(a)]. This is consistent with the behavior expected from the classical analysis of fluctuations about these spiral states in Sec. V, since it is the same set of wave vectors that is selected. The full locus of spiral wave vectors [Eq. (3) and Fig. 3]

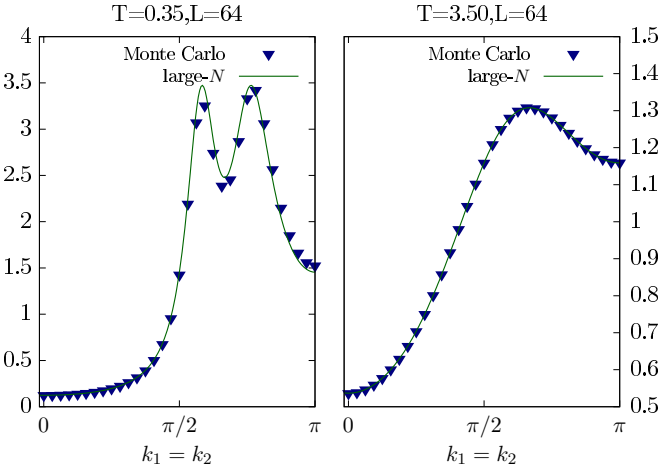

FIG. 8. Intralayer spin correlations in momentum space (y axis) obtained using classical Monte Carlo simulations of the effective model for a system of $L \times L$ unit cells with $L = 64$ are well approximated by large-N (Sec. III) results for the same quantity. The correlation functions are plotted along the cut $k_1 = k_2$ in momentum space (with out of plane momentum set to zero). The left panel shows this comparison for $T = 0.35(J/4) \simeq 100$ mK. The right panel shows the same comparison for $T = 3.50(J/4) \simeq 1$ K ($J/4 \simeq 290$ mK).

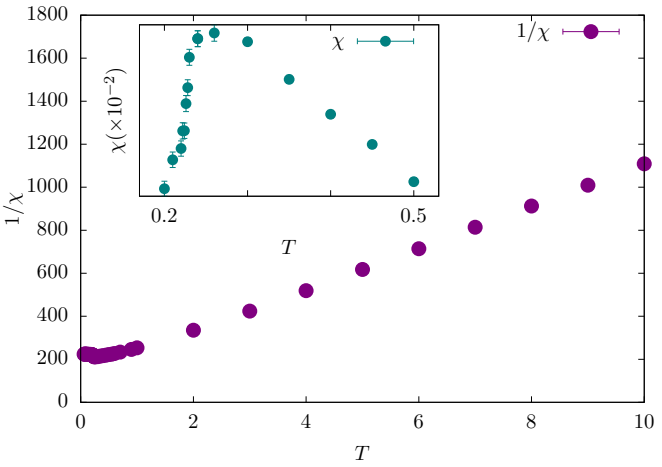

FIG. 9. Inverse susceptibility $1/\chi$ of the effective model on a lattice of $L \times L$ unit cells, with $L = 64$, plotted against temperature T expressed in units of $(J/4) \approx 290$ mK [χ is defined as in Eq. (35)]. A clear deviation from linearity is visible at low temperature. Inset: The uniform susceptibility χ at low temperature shows a crossover at a temperature roughly consistent with the peak in the specific heat data. This crossover temperature corresponds to the temperature scale at which spiral correlations start to build up (as evidenced by our results for the spin correlations and structure factor), although our spin-wave calculations at $T = 0$ strongly suggest that long-range spiral order (favored at $T = 0$ by the pattern of exchange couplings) is destabilized by singular spin-wave fluctuations. Note that the crossover scale is consistent with the position of the peak in the specific heat curve, which marks the sharp onset of nematic order in the bond energies.

obtained from large-N calculations in Sec. III become visible at somewhat higher temperature, as shown in Fig. 7(b). At even higher temperatures, the correlation function between spins in the same layer starts looking more and more liquidlike, as shown in Fig. 7(c) and Fig. 7(d). Further, the correlation functions obtained in the Monte-Carlo simulations are in reasonable agreement with the ones calculated in large N. We have displayed the agreement of our Monte-Carlo correlation functions within the same layer with the large-N results in Fig. 8. The slight disagreement at the lower temperature can be ascribed to the fact that the large-N analysis does not capture the entropic effects which lead to the selection of a particular set of spiral wave vectors at low temperatures, as described in Sec. V.

Next we compute the uniform susceptibility χ, given by

$$\chi = \frac{1}{2TL^2}\left(\left\langle \sum_i \hat{n}_i^2 \right\rangle_{\rm MC} - \left\langle \sum_i \hat{n}_i \right\rangle_{\rm MC}^2\right). \qquad (35)$$

In Fig. 9 we display results for the inverse spin susceptibility, $1/\chi$. The linear behavior at high temperature, characteristic of a paramagnet, persists down to a crossover temperature, below which deviations are apparent. [As noted in Sec. II, the linear behavior, if extrapolated down, has an antiferromagnetic intercept, which reflects the fact that we are working with an effective model of $S = 3/2$ spins, and the true high-temperature limit (at temperatures well above the large ferromagnetic exchange couplings) is not accessible to our model.] Deviations

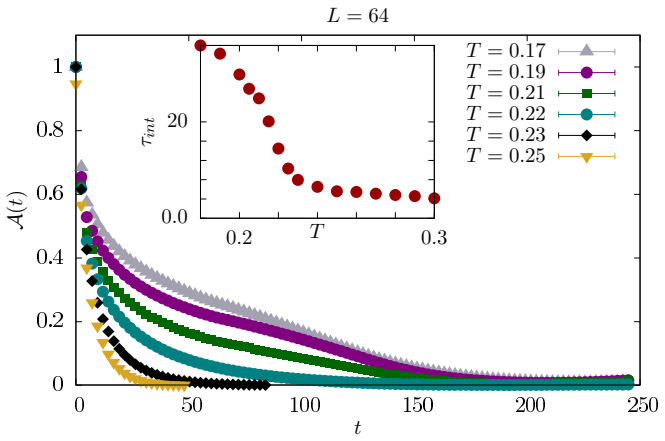

FIG. 10. Spin autocorrelation function $\mathcal{A}(t)$ of the effective model plotted as a function of t displayed in units of $(J/4)^{-1}$. Inset shows the temperature dependence of the relaxation time defined via the integrated autocorrelation function. These relaxation times show a crossover at $T_{\text{crossover}} \simeq 0.22\,(J/4) \simeq 64$ mK. The uniform susceptibility display crossovers at roughly the same temperature. As mentioned earlier, this crossover temperature corresponds to the temperature scale at which spiral correlations start to build up (as evidenced by our results on the spin correlations and structure factor), although our spin-wave calculations at $T = 0$ strongly suggest that long-range spiral order (favored at $T = 0$ by the pattern of exchange couplings) is destabilized by singular spin-wave fluctuations. Note that the crossover scale is consistent with the position of the peak in the specific heat curve, which marks the sharp onset of nematic order in the bond energies.

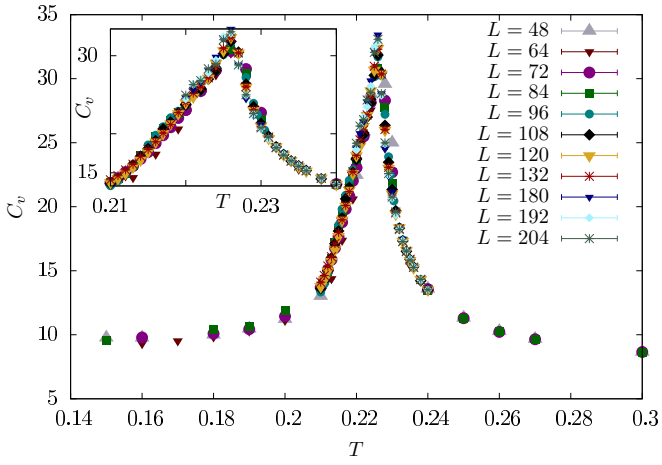

FIG. 11. Specific heat C [Eq. (38)] of the effective model on a lattice of $L \times L$ unit cells, with $L = 48$, 64, 72, 84, 96, 108, 120, 132, 180, 192, and 204, plotted against temperature T, expressed in units of $(J/4) \approx 290$ mK. There is a clear peak at a temperature $T^* \simeq 0.22\,(J/4) \simeq 64$ mK. The inset zooms in to better display the shape of the curve near the peak as well as the size dependence visible within the range of sizes studied here. As is clear from the displayed data, this peak does not scale with system size within the range studied here, apparently ruling out a phase transition. Indeed, our results appear to saturate to the thermodynamic limit already for the range of sizes studied, including at the position of the peak. However, results for the bond-energy nematic order parameter for the same range of sizes suggest the sharp onset of nematicity at a temperature corresponding to this peak (see below).

from paramagnetic behavior below the crossover scale are also apparent in the plot of the uniform susceptibility χ shown in the inset of Fig. 9. Note that the small bump in χ as a function of temperature serves as a marker for the crossover temperature, which is consistent with the crossover visible in the Fourier transform of the spin correlators discussed earlier.

Next we look at spin autocorrelation functions, defined as

$$\mathcal{A}(t) = \langle \hat{n}_i(0) \cdot \hat{n}_i(t) \rangle_{\text{MC}}. \tag{36}$$

We show the decay of spin autocorrelations in Fig. 10. At higher temperatures, the autocorrelations decay exponentially like in a paramagnet. At lower temperatures, the autocorrelation curves develop a knee and cross over to a regime of slow dynamics. To extract a time scale from these relaxation rates, we define the integrated autocorrelation time τ_{int} as

$$\tau_{\text{int}} = \int_0^\infty dt\, \mathcal{A}(t). \tag{37}$$

We plot the relaxation time scales τ_{int} obtained in this manner in the inset of Fig. 10. We see that the autocorrelation timescale shows a crossover to slow dynamics at $T_{\text{crossover}} \simeq 0.22\,(J/4)$, consistent with the crossover in the uniform susceptibility plots and the Fourier transform of the spin correlation functions.

To connect this crossover in the spin channel with the puzzling transition to nematic order in the bond energies reported earlier in Mulder *et al.* [14] for $J_2/J_1 = 1$ and nearby values, we have revisited the specific heat and nematic order parameter susceptibility of this system, going to somewhat larger sizes than in the work of Mulder *et al.* Defining the specific heat as

$$C = \frac{1}{2T^2L^2}(\langle E^2 \rangle_{\text{MC}} - \langle E \rangle_{MC}^2), \tag{38}$$

where E is the total energy of a configuration and $\langle \ldots \rangle_{\text{MCS}}$ denotes a Monte Carlo average, we have obtained the specific heat data for different system sizes shown in Fig. 11. We see a peak in the specific heat at $T \approx 0.22\,(J/4)$. However, we also note that the peak does not scale at all with the system size. Indeed, from Fig. 11, we see that linear sizes that differ by more than a factor of three give curves that overlap with each other within error bars, indicating that finite size effects are already negligible at these sizes. Note that this peak is apparently unrelated to the bump at $T \simeq 4$ K in the experimental specific heat curve reported in Ref. [9]: Indeed, as noted in Sec. II, this temperature scale seen in the experiments corresponds quite well to the average of the two energy scales (since the ferromagnetic couplings in the two layers are different) associated with the unbinding of the ferromagnetically bound effective $S = 3/2$ moments into three $S = 1/2$ moments, suggesting that this is the origin of the specific heat feature studied experimentally. Since our calculations are in terms of an effective Hamiltonian for the spin $S = 3/2$ degrees of freedom, we do not capture this higher temperature feature within our effective theory.

Turning our attention to the interpretation of the peak in the specific heat at $T \approx 0.22\,(J/4)$, we note that any interpretation of this specific heat peak in terms of a thermodynamic singularity associated with a phase transition would normally

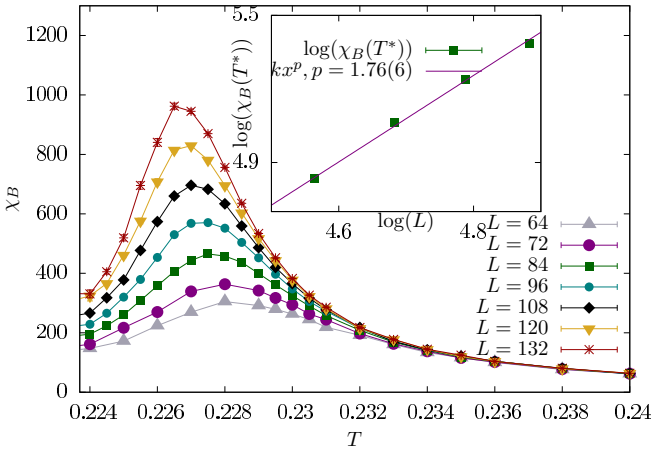

FIG. 12. Nematic order parameter susceptibility [Eq. (40)] of the effective model on a lattice of $L \times L$ unit cells, with 64, 72, 84, 96, 108, 120, and 132, plotted against temperature T, expressed in units of $(J/4) \approx 290$ mK. There is a clear peak at a temperature $T^* \simeq 0.22\,(J/4) \simeq 64$ mK. The height of this peak, plotted in the inset as a function of system size, shows the expected finite-size scaling behavior at a thermodynamic phase transition, consistent with the results of Mulder *et al.* [14]. In particular, our power-law fit (shown as a line in the inset) for the L dependence of the peak height has power-law exponent 1.76(6), consistent with the known value of $26/15 = 1.733\ldots$ for this exponent at the three-state Potts transition.

have been ruled out by the fact that the data appears to have already converged to the thermodynamic limit over the range of sizes studied. [We have also checked that the spin structure factor data (discussed below) and the equal time correlation results (displayed earlier) for spins are both reasonably well converged to the thermodynamic limit at the sizes used in our study, suggesting that this range of sizes is perfectly adequate as a means of extrapolating to the thermodynamic limit.]

However, as was already noted by Mulder *et al.* [14], when one computes for the same range of sizes the complex bond-energy nematic order parameter defined as:

$$B(\vec{r}) = \hat{n}_{1,\vec{r}} \cdot \hat{n}_{2,\vec{r}} + e^{i2\pi/3} \hat{n}_{1,\vec{r}} \cdot \hat{n}_{2,\vec{r}+\hat{e}_1} + e^{i4\pi/3} \hat{n}_{1,\vec{r}} \cdot \hat{n}_{2,\vec{r}+\hat{e}_2}, \tag{39}$$

we see behavior that is consistent with the sharp onset of nematicity at a temperature corresponding to this peak in the specific heat. This is shown in Fig. 12 where we plot the order parameter susceptibility χ_B, given by

$$\chi_B = \frac{1}{TL^2}\left(\left\langle\left|\sum_{\vec{r}} B(\vec{r})\right|^2\right\rangle_{\rm MC} - \left|\left\langle\sum_{\vec{r}} B(\vec{r})\right\rangle_{\rm MC}\right|^2\right), \tag{40}$$

over a somewhat larger range of sizes than in the previous work [14]. Clearly, we see behavior consistent with Mulder *et al.*'s identification of a transition to nematic order in the bond energies [14]. In particular, we are able to fit the height of the peak to the expected scaling behavior at the three-state Potts transition (inset of Fig. 12). More work is needed to understand this puzzling nematic transition, given that the discrepancy between the behavior of the specific heat and the order parameter susceptibility is seen to persist even at the larger sizes accessed in our study.

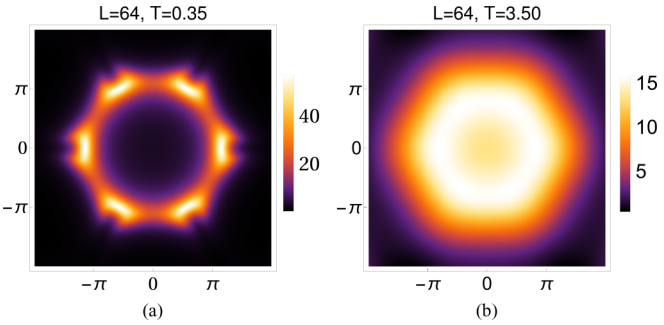

FIG. 13. In plane momentum dependence (with out of plane momentum set to zero) of the equal-time structure factor $\mathcal{S}^{\rm MC}(\vec{k})$ [Eq. (41)] of the effective model, obtained from Monte Carlo simulations of systems with $L \times L$ unit cells, with $L = 64$, for temperatures (a) $0.35(J/4) \simeq 100$ mK and (b) $3.50(J/4) \simeq 1$ K $(J/4 \simeq 290$ mK). The spiral features visible in the corresponding intralayer correlation function at the lower temperature (displayed earlier in Fig. 7) are partially smeared out due to the effect of form factors but still visible. The results at the higher temperature are largely featureless.

Independent of this puzzle, we can nevertheless conclude that the temperature of specific heat peak is roughly consistent with the crossover in the spin channel associated with a growing spiral correlation length (Fig. 7) which leaves its mark on the Fourier transform of the spin correlation function, on the uniform spin susceptibility, and on the local spin autocorrelation function.

In addition, we have also measured the equal time structure factors defined as:

$$\mathcal{S}^{\rm MC}(\vec{k}) = \frac{1}{L^2}\langle|\hat{n}_1(\vec{k}) f_1(\vec{k}) + \hat{n}_2(\vec{k}) f_2(\vec{k})|^2\rangle_{\rm MC}, \tag{41}$$

where the form factors of the effective $S = 3/2$ moments are given in Appendix D. The equal time structure factors for $T = 0.35(J/4)(\approx 100$ mK) and $T = 3.50(J/4)(\approx 1$ K) are shown in Fig. 13. At the lower temperature, we see clear evidence of spiral correlations, whereas the higher temperature results are featureless.

Finally, we have calculated the dynamic structure factor, defined as

$$\mathcal{S}^{\rm MC}(\vec{k},\omega) = \frac{1}{L^2 N_\tau}\langle|\hat{n}_1(\vec{k},\omega) f_1(\vec{k}) + \hat{n}_2(\vec{k},\omega) f_2(\vec{k})|^2\rangle_{\rm MC}. \tag{42}$$

Here, $\hat{n}_\alpha(\vec{k},\omega)$ is calculated by fast Fourier transforming $\hat{n}_{\alpha,}(r_i,t)$ obtained from the numerical integration of the Hamiltonian equations of motion (34) (N_τ is the number of steps used in numerical integration). The dynamic structure factors at $T = 0.35(J/4) \approx 100$ mK for frequencies $0.41(J/4) \approx 0.010$ meV and $1.74(J/4) \approx 0.044$ meV are shown in Fig. 14. Both these frequencies fall well within the quasielastic window of the recent inelastic neutron scattering measurements [9]. At the lower of the two frequencies, one sees clear features corresponding to low-frequency fluctuations at wave vectors on the spiral locus. At the higher frequency, the structure factor is liquidlike and relatively featureless.

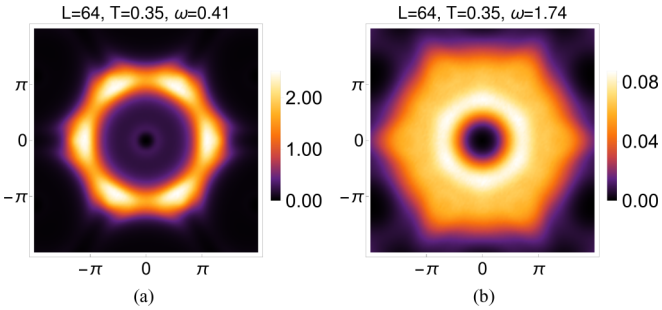

FIG. 14. Plots showing the in plane momentum dependence (with out of plane momentum set to zero) of dynamic structure factors $\mathcal{S}^{\rm MC}(\vec{k},\omega)$ defined in Eq. (42), obtained from combined Monte Carlo-molecular dynamics simulations of the effective at low temperature $T = 0.35(J/4) \simeq 100$ mK for a system of $L \times L$ unit cells with $L = 64$. (a) The dynamic structure factor at low frequency [$\omega = 0.41(J/4) \simeq 0.01$ meV] shows clear features corresponding to low-frequency fluctuations at wave vectors on the spiral locus. (b) The dynamic structure factor at a somewhat higher frequency $\omega = 1.74(J/4) \simeq 0.0435$ meV (which is still very low compared to the scale at which inelastic neutron scattering experiments have probed the dynamics) is already featureless ($J/4 \approx 290$ mK). Note that recent experiments have probed the dynamic structure factor mainly at significantly higher frequencies ($\gtrsim$0.25 meV), which actually correspond in our picture to the natural energy scale for transitions of the strongly coupled ferromagnetic triangles from the total spin $S = 3/2$ multiplet to the higher energy $S = 1/2$ doublets.

VII. DISCUSSION

The analysis presented here strongly suggests that the low temperature behavior of $Ca_{10}Cr_7O_{28}$ provides an interesting example of a frustrated magnet in which the exchange couplings favor $T = 0$ incommensurate spiral order. The presence of singular spin-wave fluctuations at wave vectors in the vicinity of the locus of spiral wave vectors also suggests that spiral order is unstable at $T = 0$ due to these fluctuations, although this leading order spin-wave result itself could get modified by a nonperturbative treatment of $1/S$ corrections. Independent of the fate of the system at $T = 0$, we show that there is a nonzero temperature crossover to a regime in which the spin autocorrelation time scale, equal time spin correlations, and the dynamic spin structure factor all reflect the presence of a large but finite correlation length for spiral spin correlations at a particular set of entropically selected zone boundary spiral wave vectors. The temperature scale for this crossover is roughly the same as the onset temperature for nematicity in the bond energies, seen in earlier work [14].

Our numerical results suggest that this crossover temperature is $T_{\rm crossover} \simeq 0.22\,(J/4) \simeq 64$ mK—this is small because it is set by the relatively weak effective interactions between the effective $S = 3/2$ degrees of freedom. The corresponding frequency scale (at which dynamical fluctuations at spiral wave vectors become apparent) is $\omega_{\rm crossover} \simeq 0.4(J/4) \simeq 0.01$ mev, which falls well within the "quasistatic" window of inelastic neutron scattering studies of $Ca_{10}Cr_7O_{28}$ [9]. These recent experiments have also largely focused on the physics in a somewhat higher temperature window ($T \gtrsim 100$ mK) which is, by our reckoning, significantly above the crossover temperature at which the buildup of spiral correlations could be seen. In this higher temperature window, our results are quite consistent with the liquidlike behavior seen in the experiments. In this context, we emphasize that our analysis, which focuses on the physics of the low-energy effective theory, cannot address the physics of the higher temperature crossover, corresponding to the "binding" of the ferromagnetic triangles into the $S = 3/2$ effective moments that form the basic degrees of freedom at lower temperatures. From a comparison of the relevant energy scales, it appears that at least some of the features seen in the recent inelastic neutron scattering data on $Ca_{10}Cr_7O_{28}$ may be ascribed to the physics of transitions from the low energy $S = 3/2$ multiplet to higher energy doublets in the spectrum of the ferromagnetically coupled triangles in each layer. We hope our results provide some stimulus for future experiments that explore the physics of the crossover to the low temperature regime dominated by the onset of spiral correlations.

Note added. Recently, we became aware of a parallel study [34] that also addresses the physics of $Ca_{10}Cr_7O_{28}$, and it would be interesting to compare and contrast our conclusions with those of this parallel study.

ACKNOWLEDGMENTS

We thank ICTS-TIFR Bengaluru for hospitality during the School on Current Frontiers in Condensed Matter Research 2016, where the initial part of this study was completed. Our subsequent computational work at the TIFR was made possible by the computational resources of the Department of Theoretical Physics of the Tata Institute of Fundamental Research, as well as by computational resources funded by DST (India) Grant No. DST-SR/S2/RJN-25/2006. We gratefully acknowledge the hospitality of the Institute of Solid State Physics at the Univeristy of Tokyo (Kashiwa), where this draft was finalized for submission.

APPENDIX A: DETAILS OF SPIN-WAVE CALCULATION

The expressions for the matrix $\mathbf{M}(\vec{q},\vec{k})$ and $a(\vec{q},\vec{k})$ in Eq. (20) are given here. In the rest of this section, we suppress all explicit $\vec{q}$ dependences in our notation for convenience. Thus we write

$$\mathbf{M}(\vec{q},\vec{k}) = \begin{pmatrix} \mathbf{A}(\vec{k}) & \mathbf{B}(\vec{k}) \\ \mathbf{B}(\vec{k}) & \mathbf{A}(\vec{k}) \end{pmatrix}. \tag{A1}$$

The 2×2 matrices $\mathbf{A}$ and $\mathbf{B}$ are given by

$$\mathbf{A}(\vec{k}) = J^{\rm eff} \begin{pmatrix} a(\vec{k}) & c^*(\vec{k}) \\ c(\vec{k}) & a(\vec{k}) \end{pmatrix} \tag{A2}$$

$$\mathbf{B}(\vec{k}) = J^{\rm eff} \begin{pmatrix} b(\vec{k}) & d^*(\vec{k}) \\ d(\vec{k}) & b(\vec{k}) \end{pmatrix}. \tag{A3}$$

The matrix elements are given by

$$\begin{aligned} a(\vec{k}) = {} & (\cos(q_1)+1)\cos(k_1) + (\cos(q_2)+1)\cos(k_2) \\ & + (\cos(q_1+q_2)+1)\cos(k_1+k_2) \\ & + (\cos(\theta_{\vec{q}}) + \cos(\theta_{\vec{q}} - q_1) + \cos(\theta_{\vec{q}} - q_1 - q_2)) \\ & - 2(\cos(q_1) + \cos(q_2) + \cos(q_1+q_2)) \end{aligned}$$

$$b(\vec{k}) = (\cos(q_1) - 1)\cos(k_1) + (\cos(q_2) - 1)\cos(k_2) + (\cos(q_1 + q_2) - 1)\cos(k_1 + k_2)$$

$$c(\vec{k}) = -\frac{1}{2}((\cos(\theta_{\vec{q}}) + 1) + (\cos(\theta_{\vec{q}} - q_1) + 1)e^{ik_1} + (\cos(\theta_{\vec{q}} - q_1 - q_2) + 1)e^{i(k_1+k_2)})$$

$$d(\vec{k}) = -\frac{1}{2}((\cos(\theta_{\vec{q}}) - 1) + (\cos(\theta_{\vec{q}} - q_1) - 1)e^{ik_1} + (\cos(\theta_{\vec{q}} - q_1 - q_2) - 1)e^{i(k_1+k_2)}).$$

The spin-wave dispersions $E_{\pm}^{\mathrm{SW}}(\vec{k})$ of Eq. (22) can be obtained by solving the auxiliary eigenproblem

$$(\mathbf{A}(\vec{k}) + \mathbf{B}(\vec{k}))(\mathbf{A}(\vec{k}) - \mathbf{B}(\vec{k}))\Psi = (E^{\mathrm{SW}}(\vec{k}))^2\Psi. \tag{A4}$$

Solving this, we find that the dispersions of the spin-wave modes are given by

$$E_{\pm}^{\mathrm{SW}}(\vec{k}) = J^{\mathrm{eff}}\sqrt{\lambda_1(\vec{k}) \pm \lambda_2(\vec{k})}, \tag{A5}$$

$$\lambda_1(\vec{k}) = a(\vec{k})^2 - b(\vec{k})^2 + |c(\vec{k})|^2 - |d(\vec{k})|^2, \tag{A6}$$

$$\lambda_2(\vec{k}) = \sqrt{4|a(\vec{k})c(\vec{k}) - b(\vec{k})d(\vec{k})|^2 + (c(\vec{k})d(\vec{k})^* - c(\vec{k})^*d(\vec{k}))}. \tag{A7}$$

APPENDIX B: ENTROPIC SELECTION OF GROUND STATES AT LOW TEMPERATURES

As mentioned in Sec. V, the matrix $K(\vec{q})$, where $\vec{q}$ is the wave vector of the spiral ground state about which fluctuations are studied, is block diagonal in Fourier space. The 2×2 blocks, labeled by the Fourier component $\vec{k}$ of the fluctuation, may be written as

$$\mathbf{K}(\vec{q},\vec{k}) = J^{\mathrm{eff}}|S|^2\begin{pmatrix} e(\vec{k}) & f^*(\vec{k}) \\ f(\vec{k}) & e(\vec{k}) \end{pmatrix}, \tag{B1}$$

where the explicit $\vec{q}$ dependence of e and f have been suppressed. The functions $e(\vec{k})$ and $f(\vec{k})$ are given by

$$e(\vec{k}) = (\cos(q_1) + 1)\cos(k_1) + (\cos(q_2) + 1)\cos(k_2) + (\cos(q_1 + q_2) + 1)\cos(k_1 + k_2) + \frac{1}{2}(\cos(\theta_{\vec{q}}) + \cos(\theta_{\vec{q}} - q_1) + \cos(\theta_{\vec{q}} - q_1 - q_2))$$

$$f(\vec{k}) = -\frac{1}{2}(\cos(\theta_{\vec{q}}) + \cos(\theta_{\vec{q}} - q_1)e^{ik_1} + \cos(\theta_{\vec{q}} - q_1 - q_2)e^{i(k_1+k_2)}).$$

The eigenvalues of the 2×2 matrix $K(\vec{k},\vec{q})$ are given by $J^{\mathrm{eff}}|S|^2(e(\vec{k}) \pm |f(\vec{k})|)$.

APPENDIX C: DETAILS OF MONTE-CARLO UPDATES

Following Young *et al.* [31], we have used three different updates in our Monte Carlo:

(a) *Over-relaxation moves*: These are energy conserving moves where a spin $\vec{S}_i$ is randomly selected and reflected about local exchange field $\vec{H}_i$ induced by the coupling to other spins, with

$$\vec{H}_i = \sum_j M_{ij}\vec{S}_j. \tag{C1}$$

This reflection is implemented by

$$\vec{S}_i \rightarrow \vec{S}_i - \frac{2\vec{S}_i.\vec{H}_i}{|\vec{H}_i|}. \tag{C2}$$

Over-relaxation moves help the simulations to equilibrate faster.

(b) *Heat-bath moves*: Over-relaxation moves described above are microcanonical and therefore not ergodic. So, we supplement them with heat-bath moves. We randomly select a spin $\vec{S}_i$ and choose a new azimuthal angle θ and polar angle ϕ to specify its orientation relative to the local magnetic field $\vec{H}_i$ defined in Eq. (C1). The new angle θ is chosen with the *heat-bath* probability $P(\cos(\theta))$, given by

$$P(\cos(\theta)) = \frac{\beta|\vec{H}_i|}{\sin(\beta|\vec{H}_i|)}\exp(-\beta|\vec{H}_i|\cos(\theta)). \tag{C3}$$

As is well known, $\cos(\theta)$ can be drawn from the above distribution by drawing a random number r from a uniform distribution and equating it to the corresponding cumulative distribution. This prescription yields a random value for $\cos(\theta)$ in terms of the random number r:

$$\cos(\theta) = -\frac{1}{\beta|\vec{H}|}\log(1 + r\exp(-2\beta|\vec{H}|)). \tag{C4}$$

If the azimuthal and polar angles made by the local field $\vec{H}$ with the co-ordinate axes are θ' and ϕ', respectively, the spin with orientation (θ,ϕ) with respect to the effective magnetic field $\vec{H}$ can be written in our global coordinate system as:

$$S_x = \cos(\theta)\sin(\theta')\cos(\phi') \tag{C5}$$
$$+ \sin(\theta)\cos(\phi)\sin(\phi') \tag{C6}$$
$$+ \sin(\theta)\sin(\phi)\cos(\theta')\cos(\phi') \tag{C7}$$
$$S_y = \cos(\theta)\sin(\theta')\sin(\phi') - \sin(\theta)\cos(\phi)\cos(\phi') \tag{C8}$$
$$+ \sin(\theta)\sin(\phi)\cos(\theta')\sin(\phi') \tag{C9}$$
$$S_z = \cos(\theta')\cos(\theta) - \sin(\theta')\sin(\theta)\sin(\phi). \tag{C10}$$

(c) *Parallel Tempering*: Finally, we use parallel tempering or replica exchange to improve equilibration and eliminate loss of ergodicity at very low temperatures. We simultaneously run independent Monte Carlo simulations at a series of temperatures such that the highest few temperatures are high enough to not suffer from any loss of ergodicity. In a replica exchange move, one takes equilibriated configurations from independent simulations at T_1 and T_2 and exchanges the system

configurations in their entirety between the two simulations, using an acceptance probability that obeys detailed balance

$$P(T_1 \leftrightarrow T_2) = W_f/W_i, \quad \text{for } W_f < W_i \tag{C11}$$

$$= 1, \quad \text{otherwise.} \tag{C12}$$

The ratio of the weights W_f/W_i is given in terms of the energies of the configurations E_1 and E_2 as

$$W_f/W_i = e^{-\frac{1}{T_1}(E_2-E_1)} e^{-\frac{1}{T_2}(E_1-E_2)}. \tag{C13}$$

Clearly, this is equivalent in practice to simply exchanging the temperatures of the two independent simulations before restarting both of them, and this is what is done in practice.

APPENDIX D: FORM FACTORS FOR $S = 3/2$ MOMENTS

The form factors $f_1(\vec{k})$ and $f_2(\vec{k})$ for the effective $S = 3/2$ degrees of freedom are given by

$$f_1(\vec{k}) = (1 + e^{ik_1/2} + e^{-ik_2/2}) e^{i(-k_1/6)+i(k_2/6)}, \tag{D1}$$

$$f_2(\vec{k}) = (1 + e^{ik_1/2} + e^{i(k_1/2)+i(k_2/2)}) e^{i(-k_1/3)+i(-k_2/6)} \times e^{i(2k_1/3)+i(k_2/3)} \times e^{ik_3 d_z}, \tag{D2}$$

where d_z is the ratio of the interlayer separation to the distance between two unit cells of the triangular Bravais lattice of the effective model. This number is never actually needed for our purposes because we calculate momentum dependent quantities like structure factors with the out of plane momentum k_3 set to zero.

[1] L. Balents, Spin liquids in frustrated magnets, Nature (London) **464**, 199 (2008).

[2] L. Savary and L. Balents, Quantum spin liquids: A review, Rep. Prog. Phys. **80**, 016502 (2017).

[3] A. Sen, K. Damle, and R. Moessner, Fractional Spin Textures in the Frustrated Magnet $SrCr_{9p}Ga_{12-9p}O_{19}$, Phys. Rev. Lett. **106**, 127203 (2011).

[4] A. Sen, K. Damle, and R. Moessner, Vacancy-induced spin textures and their interactions in a classical spin liquid, Phys. Rev. B **86**, 205134 (2012).

[5] P. Schiffer and I. Daruka, Two-population model for anomalous low-temperature magnetism in geometrically frustrated magnets, Phys. Rev. B **56**, 13712 (1997).

[6] L. Limot *et al.*, Susceptibility and dilution effects of the kagomé bilayer geometrically frustrated network: A Ga NMR study of $SrCr_{9p}Ga_{12-9p}O_{19}$, Phys. Rev. B **65**, 144447 (2002).

[7] P. A. Lee, An end to the drought of quantum spin liquids, Science **321**, 1306 (2008).

[8] A. P. Ramirez, Quantum spin liquids: A flood or a trickle? Nat. Phys. **4**, 442 (2008).

[9] C. Balz *et al.*, Physical realization of a quantum spin liquid based on a complex frustration mechanism, Nat. Phys. **12**, 942 (2016).

[10] C. Balz *et al.*, The magnetic hamiltonian and phase diagram of the quantum spin liquid $Ca_{10}Cr_7O_{28}$, Phys. Rev. B **95**, 174414 (2017).

[11] R. Moessner and J. T. Chalker, Properties of a Classical Spin Liquid: The Heisenberg Pyrochlore Antiferromagnet, Phys. Rev. Lett. **80**, 2929 (1998).

[12] R. Moessner and J. T. Chalker, Low-temperature properties of classical geometrically frustrated antiferromagnets, Phys. Rev. B **58**, 12049 (1998).

[13] K. Momma and F. Izumi, Vesta 3 for three-dimensional visualization of crystal, volumetric and morphology data, J. Appl. Crystallogr. **44**, 1272 (2011).

[14] A. Mulder, R. Ganesh, L. Capriotti, and A. Paramekanti, Spiral order by disorder and lattice nematic order in a frustrated Heisenberg antiferromagnet on the honeycomb lattice, Phys. Rev. B **81**, 214419 (2010).

[15] S. Okumura, H. Kawamura, T. Okubo, and Y. Motome, Novel spin-liquid states in the frustrated Heisenberg antiferromagnet on the honeycomb lattice, J. Phys. Soc. Jpn. **79**, 114705 (2010).

[16] E. Rastelli, A. Tarsi, and L. Reatto, Non-simple magnetic order for simple Hamiltonians, Physica B **97**, 1 (1979).

[17] J. B. Fouet, P. Sindzingre, and C. Lhuillier, An investigation of the quantum $J1 - J2 - J3$ model on the honeycomb lattice, Eur. Phys. J. B **20**, 241 (2001).

[18] A. Mattsson, P. Fröjdh, and T. Einarsson, Frustrated honeycomb Heisenberg antiferromagnet: A Schwinger-boson approach, Phys. Rev. B **49**, 3997 (1994).

[19] R. Ganesh, D. N. Sheng, Y. J. Kim, and A. Paramekanti, Quantum paramagnetic ground states on the honeycomb lattice and field-induced Néel order, Phys. Rev. B **83**, 144414 (2011).

[20] M. L. Baez and J. Reuther, Numerical treatment of spin systems with unrestricted spin length S: A functional renormalization group study, Phys. Rev. B **96**, 045144 (2017).

[21] S. K. Ma, *Modern Theory of Critical Phenomena*, Advanced Book Classics (Westview Press, Boulder, USA, 2000).

[22] D. A. Garanin and B. Canals, Spin-liquid phase in the pyrochlore anti-ferromagnet, Can. J. Phys. **79**, 1323 (2001).

[23] D. A. Garanin and B. Canals, Classical spin liquid: Exact solution for the infinite-component antiferromagnetic model on the kagome lattice, Phys. Rev. B **59**, 443 (1999).

[24] F. Wang, A. Vishwanath, and Y. B. Kim, Quantum and classical spins on the spatially distorted Kagomé lattice: Applications to volborthite $Cu_3V_2O_7(OH)_2\dot{H}_2O$, Phys. Rev. B **76**, 094421 (2007).

[25] S. V. Isakov, K. Gregor, R. Moessner, and S. L. Sondhi, Dipolar Spin Correlations in Classical Pyrochlore Magnets, Phys. Rev. Lett. **93**, 167204 (2004).

[26] J. M. Luttinger and L. Tisza, Theory of dipole interaction in crystals, Phys. Rev. **70**, 954 (1946).

[27] J. H. P. Colpa, Diagonalization of the quadratic boson Hamiltonian with zero modes, Physica A **134**, 417 (1986).

[28] D. Bergman, J. Alicea, E. Gull, S. Trebst, and L. Balents, Order-by-disorder and spiral spin-liquid in frustrated diamond-lattice antiferromagnets, Nat. Phys. **3**, 487 (2007).

[29] U. Wolff, Collective Monte Carlo Updating for Spin Systems, Phys. Rev. Lett. **62**, 361 (1989).

[30] M. Hasenbusch, Improved estimators for cluster updating of $O(n)$ spin models, Nucl. Phys. B **333**, 581 (1990).

[31] L. W. Lee and A. P. Young, Large-scale Monte Carlo simulations of the isotropic three-dimensional Heisenberg spin glass, Phys. Rev. B **76**, 024405 (2007).

[32] J. H. Pixley and A. P. Young, Large-scale Monte Carlo simulations of the three-dimensional XY spin glass, Phys. Rev. B **78**, 014419 (2008).

[33] A. Keren, Dynamical Simulation of Spins on Kagomé and Square Lattices, Phys. Rev. Lett. **72**, 3254 (1994).

[34] R. Pohle, H. Yan, and N. Shannon, arXiv:1711.03778.